RAA 2017 Vol. **17** No. **8**, 77 (12pp) doi: 10.1088/1674–4527/17/8/77

http://www.raa-journal.org *http://iopscience.iop.org/raa*

Research in Astronomy and Astrophysics

Multi-transition study of the peculiar merger Arp 299

Qian Jiao[1,2,3] and Ming Zhu[1,2]

[1] National Astronomical Observatories, Chinese Academy of Sciences, Beijing 100012, China; *mz@bao.ac.cn*
[2] Key Laboratory of Radio Astronomy, Chinese Academy of Sciences, Beijing 100012, China
[3] University of Chinese Academy of Sciences, Beijing 100049, China

Received 2016 December 8; accepted 2017 April 7

Abstract We present a multi-transition study to investigate the physical properties of dust and molecular gas in the archetypical merger Arp 299 by using data including James Clerk Maxwell Telescope (JCMT) 850 and 450 μm observations, Herschel 500, 350, 250, 160 and 70 μm continuum maps, as well as the CO(3–2), CO(4–3) low-J CO lines and CO(11–10), CO(13–12), CO(14–13) high-J CO lines. The CO(3–2) and CO(4–3) lines are observed by JCMT, and the CO(11–10), CO(13–12), CO(14–13) lines are available on the Herschel Science Archive. The resolution of the Herschel Spectral and Photometric Imaging Receiver (SPIRE) Fourier transform spectrometer (FTS) CO(11–10) data is similar to that of the JCMT CO(3–2) line, while the resolution of the SPIRE/FTS CO(13–12) and Photodetector Array Camera and Spectrometer (PACS) CO(14–13) data is similar to that of JCMT CO(4–3), allowing us to obtain accurate line ratios of $I_{\rm CO(11-10)}/I_{\rm CO(3-2)}$, $I_{\rm CO(13-12)}/I_{\rm CO(4-3)}$ and $I_{\rm CO(14-13)}/I_{\rm CO(4-3)}$. By modeling the spectral energy distribution of the continuum data, we conclude that two components (cold and warm) exist in the dust, with the warm component occupying a small percent of the total dust mass. We further use a radiative transfer analysis code, RADEX, to calculate the density, temperature and column density of warm gas in the central region, which shows that the kinetic temperature $T_{\rm kin}$ is in the range 110 to 150 K and hydrogen density $n({\rm H_2})$ is in the range $10^{4.7} - 10^{5.5}\,{\rm cm^{-3}}$. We show that the hot dust is located in the central region of IC 694 with a radius of $\sim 4''$ and estimate that the warm gas mass is in the range $3.8 \times 10^7\,M_\odot$ to $7.7 \times 10^7\,M_\odot$, which contains 5.0%–15.0% of the total H_2 mass for the region of IC 694. We also calculate the star formation rate of the galaxy in particular, which is much higher than that of the Milky Way.

Key words: galaxies: merge — galaxies: Arp 299 — galaxies: dust — galaxies: molecular gas — galaxies: warm center

1 INTRODUCTION

Luminous infrared galaxies (LIRGs), with $L_{\rm IR}(8 - 1000\ \mu{\rm m}) > 10^{11}\ L_\odot$, are galaxies having intense infrared emission (Soifer et al. 1987). Typically, LIRGs contain some of the most extreme star formation systems (Papadopoulos et al. 2012). Arp 299 (NGC 3690 + IC 694, VV 118, IRAS 11257+5850, Mrk 171,UGC6471/2) is one of the nearest (46 Mpc) LIRG ($L_{\rm IR} = 5.5 \times 10^{11}\,L_\odot$ (Sanders et al. 2003)) mergers and has been the subject of detailed study. Arp 299 is made up of three main components and is dominated by intense star formation (Alonso-Herrero et al. 2000). H_α and near-infrared (NIR) images reveal extensive starburst activity in this system (García-Marín et al. 2006) and the star formation rate is about 70 $M_\odot\,{\rm yr}^{-1}$ (Sliwa et al. 2012). Single-dish observations of CO show that Arp 299 is very rich in molecular gas, and the ^{12}CO/^{13}CO line intensity ratios are extraordinarily high at both the J=1–0 and 2–1 transitions (e.g. Aalto et al. 1991, Casoli et al. 1992, Casoli et al. 1999, Sliwa et al. 2012). Such a high ratio has also been found in a few LIRG mergers like Arp 220 and NGC 6240, but has never been observed in normal spiral galaxies (NSGs). This property indicates an extreme gas environment in these merging galaxies and may have a significant bearing on their starburst activity. Aperture synthesis HCN(1–0) maps of Arp 299 (Casoli et al. 1999) show that the line intensity ratio of HCN(1–0)/CO(1–0) is also much larger than that of NSGs at the nuclear region of IC 694, which signifies that IC 694 has a large amount of molecular gas in a dense phase because HCN (with a critical density $2.6 \times 10^6\,\mathrm{cm}^{-3}$; Carolan et al. 2009) is a high density gas tracer. Mashian et al. (2015) showed that the low-J and high-J CO lines arise from two components with the same kinetic temperature of 200 K but different H_2 number densities, typically $10^{3.4}\,\mathrm{cm}^{-3}$ and $10^{5.8}\,\mathrm{cm}^{-3}$ for IC 694, and the high-J CO lines are from the dense component. The physical conditions of molecular gas, especially high density gas traced by high-J CO lines, are crucial in understanding the star formation activity in this system. The main purpose of our study is to determine the physical properties of the warm and dense molecular gas in the galactic nucleus of IC 694, as well as the distribution and properties of dust in the complete system (Arp 299).

Throughout the paper, we use data from the James Clerk Maxwell Telescope (JCMT) (850, 450 µm, CO(3–2) and CO(4–3) lines), as well as data from the Herschel Spectral and Photometric Imaging Receiver (SPIRE; Griffin et al. 2010) and Photodetector Array Camera and Spectrometer (PACS; Poglitsch et al. 2010) on board the Herschel Space Observatory (Herschel; Pilbratt et al. 2010) (500, 350, 250, 160 and 70 µm, CO(11–10), CO(13–12), CO(14–13) lines). We study in detail the spectral energy distribution (SED) of the dust based on continuum data, as well as an excitation analysis of the warm center of IC 694 by using high-J CO data. In Section 2, we give a description of the observed data. The results and discussion are presented in Section 3. Section 4 is the conclusions.

2 OBSERVATIONS

2.1 The JCMT CO(3–2) Observations

We used the JCMT on Mauna Kea, Hawaii, to observe the CO(3–2) line emission toward the starburst galaxy Arp 299 during periods in July 1999 and June 2002. The receiver B3 was tuned to single side band (SSB) to observe the spectral line with the Digital Autocorrelation Spectrometer (DAS) at a 920 MHz bandwidth. There are 13 observed points with a $\Delta\theta = 1/2\,\theta_{\rm HPBW} = 7''$ sampling, which covers most of the dust emission region from Arp 299.

The 13 observed points of CO(3–2) were centered at right ascension (RA): $11^{\rm h}28^{\rm m}32.5^{\rm s}$ and declination (Dec): $58°33'46''$. For the center and near central points, the system temperatures are $T_{\rm sys} \sim 350 - 450\,\mathrm{K}$ with $\Delta t_{\rm int} \sim 15 - 25\,\mathrm{min}$ for each point. While for the outer region, the system temperatures are $T_{\rm sys} \sim 700 - 800\,\mathrm{K}$ and $\Delta t_{\rm int} \sim 10 - 20\,\mathrm{min}$. During the grid observations, the center point at RA: $11^{\rm h}28^{\rm m}32.5^{\rm s}$ and Dec: $58°33'46''$ was repeatedly observed in order to verify pointing and line calibration. The reduced spectral profile with a calibration uncertainty of $\sim 10\%$ is shown in Figure 1, where the pointing centers are marked as P1 to P13. Compared with data from the JCMT archive observed using the new multi-beam Heterodyne Array Receiver (HARP), we found that our data observed with the single-beam B3 receiver have higher signal-to-noise ratios (S/Ns) due to longer integration time at each point. Furthermore, the B3 data are more uniform, as all points were observed with the same receiver, which makes them ideal for quantitative analysis.

2.2 The JCMT CO(4–3) Observations

Observations of the CO(4–3) transition were conducted in May 2005, mainly on the nuclear part of IC 694. The receiver D3 was tuned to SSB to observe the CO(4–3) spectral line with the DAS at a 920 MHz bandwidth. There are a total of six observed points with a $\Delta\theta = 1/2\,\theta_{\rm HPBW} = 5''$ sampling for each point. They are centered at RA: $11^{\rm h}28^{\rm m}33.6^{\rm s}$, Dec: $58°33'47''$. The system temperatures were $T_{\rm sys} \sim 3000 - 4000\,\mathrm{K}$ with $\Delta t_{\rm int} \sim 5 - 10\,\mathrm{min}$ for each point. The reduced spectra are shown in Figure 2 with a spectral line calibration uncertainty of $\sim 15\%$, on which P1 to P6 are the respective centers of the observed points. The point P5 at RA: $11^{\rm h}18^{\rm m}33.6^{\rm s}$, Dec: $58°33'47''$ has no obvious CO(4–3) emission line so we do not show its spectrum in the figure.

2.3 Dust Continuum Submillimeter Observations with SCUBA

We used the Submillimeter Common-User Bolometric Array (SCUBA) to observe 450 and 850 µm of Arp 299 in 1998 March 28 and November 24 with grade 1 and 2 weather, respectively. The submillimeter bolometer array of SCUBA contains 91 bolometers at 450 µm and 37 at 850 µm, and covers a region $\sim 2.3'$ in diameter. The secondary mirror was moved in a 64-step jiggle pattern with 1 second integration time for each point to provide

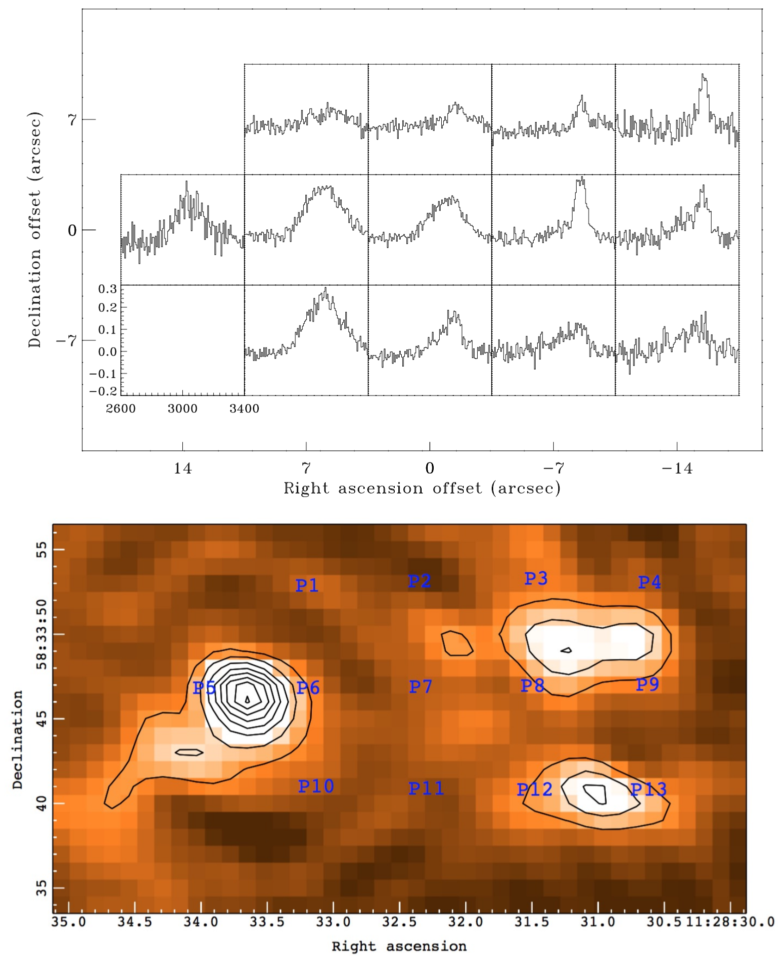

Fig. 1 The CO(3–2) data obtained for Arp 299 at a sampling of 7″ with the observed center in RA: $11^{\mathrm{h}}28^{\mathrm{m}}32.5^{\mathrm{s}}$, Dec: $58°33'46''$. The observed points are overlaid on the CO(1–0) map (Casoli et al. 1999) with contours of 1.0, 2.0, 3.0, 4.0, 5.0, 6.0, 7.0 and 8.0 Jy $\mathrm{km\,s^{-1}}$. P1 to P13 are centers of the observed points.

fully sampled images. To remove background emissions which have a slowly varying gradient, the telescope nods with a chop throw of 60″ every 1 min in the standard jiggle pattern.

We used the SURF (Jenness & Lightfoot 1998) software package to reduce the data. Atmospheric absorption was corrected using opacities which were derived from sky dip measurements. Moreover, we flagged the noisy bolometers and removed large spikes. We mapped several calibration sources to flux calibrate the images in each night. The jiggle maps were co-added in the end, and we made a final map for the complete source Arp 299 after proper data reduction. For the 450 µm observations, we only used data which were taken in grade 1 weather with sufficient S/Ns. The final maps were in units of Jy beam^{-1} with the beam profiles acquired from the CRL618 beam maps. Typically, we estimate an uncertainty of 20% in the obtained fluxes at 850 and 450 µm.

2.4 Other Continuum and Spectroscopic Data

We also used the Herschel PACS 70, 160 µm and SPIRE 250, 350, 500 µm continuum maps, which are available on the Herschel Science Archive. The SPIRE data and PACS data were observed as part of the project "Star Formation And Activity In Infrared Bright Galaxies At $0 < z < 1$." We adopted a 9.5% (Bertincourt et al. 2016) calibration uncertainty for the extended SPIRE emission data. The calibration uncertainty for the PACS data was approximately 7% (e.g. Balog et al. 2014; Nielbock et al. 2013). The data were reduced by standard pipelines with Herschel Interactive Processing

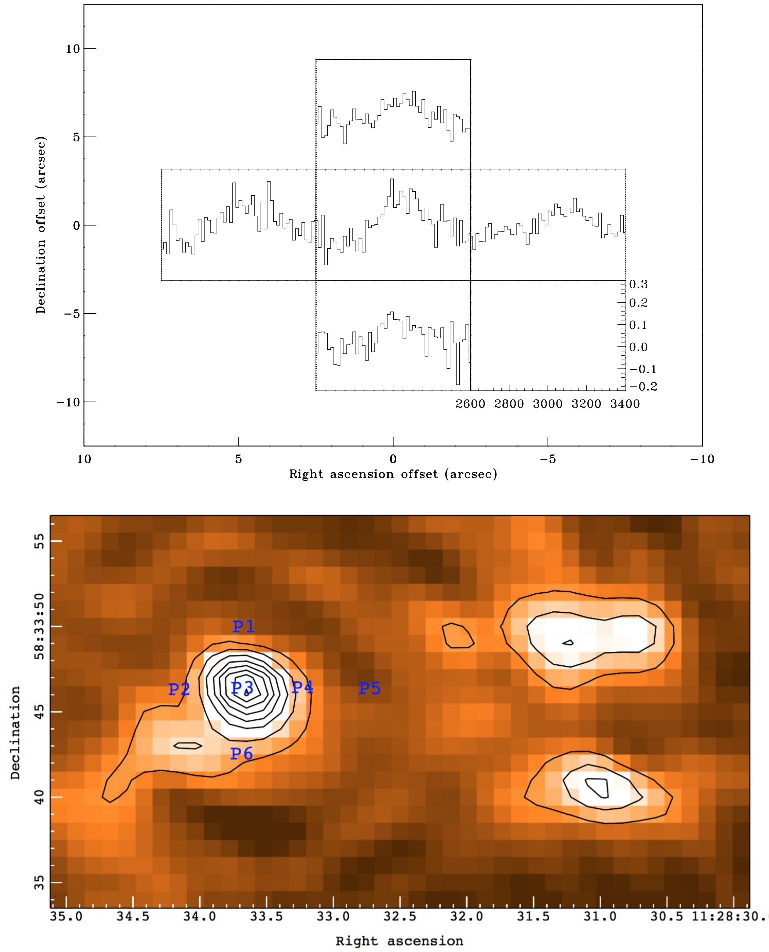

Fig. 2 The CO(4–3) data obtained for Arp 299 at a sampling of 5″ with the observed center in RA: $11^{h}28^{m}33.6^{s}$, Dec: $58^{\circ}33'47''$. The observed positions are overlaid on the CO(1–0) map (Casoli et al. 1999) with contours of 1.0, 2.0, 3.0, 4.0, 5.0, 6.0, 7.0 and 8.0 Jy $\mathrm{km\ s^{-1}}$. P1 to P6 are the centers of the observed points.

Environment (HIPE) software. Meanwhile, we also used the IRAM Plateau de Bure (PDB) interferometer CO(1–0) data (Casoli et al. 1999) and Herschel CO(11–10), CO(13–12), CO(14–13) data (Mashian et al. 2015), as well as the ISOCAM 15 μm (Gallais et al. 1999), NASA Infrared Telescope Facility (IRTF) 20, 25, 32 μm (Wynn-Williams et al. 1991) and Kuiper Widefield Infrared Camera (KWIC) 37 μm continuum data (Charmandaris et al. 2002). The details are shown in Charmandaris et al. (2002, Table 1).

3 RESULTS

3.1 Dust Emission and Temperature

Figure 3 presents the Herschel and SCUBA continuum maps with the contours of CO(1–0) integrated intensity overlaid on them. Arp 299 is a merger system with two galaxies, e.g. IC 694 in the east and NGC 3690 in the west. Following the notation of Gehrz et al. (1983), we denote the nucleus of IC 694 as source A. NGC 3690 is composed of source B in the south and source C in the north. The top panels (SCUBA 450 μm on the left and SCUBA 850 μm on the right) and the middle panels (PACS 70 μm on the left and PACS 160 μm on the right) show that the dust emission of source A is slightly stronger than that of sources B and C. The PACS 70 and 160 μm emission in the nuclei looks quite similar to that of CO(1–0), especially the dust emission centered on the IC 694 nucleus. The SCUBA 450 and 850 μm emission in the nuclei also seems to be similar to the CO(1–0) peaks, with a small offset which may be caused by the pointing error or relatively poor resolution. It appears that

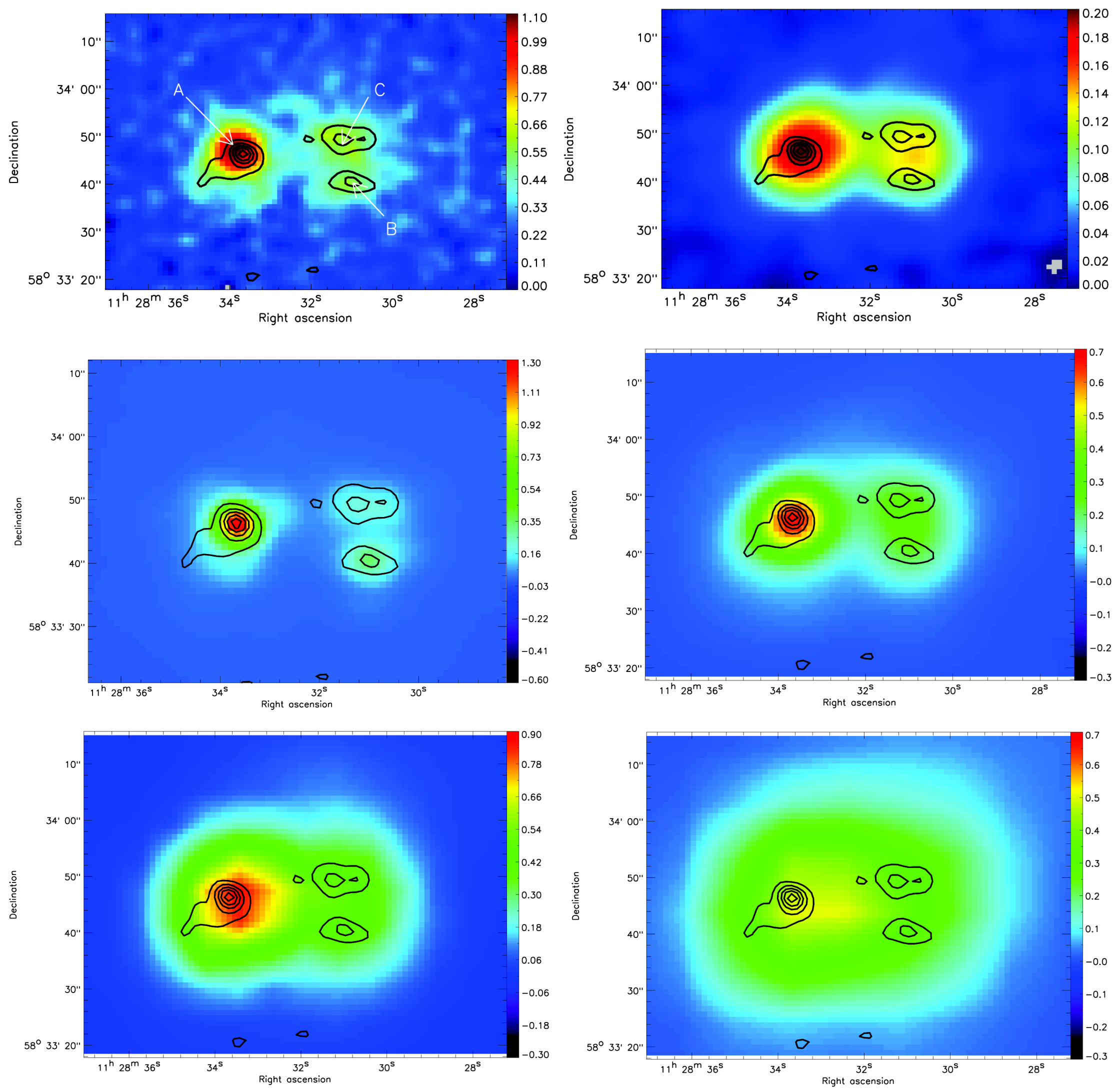

Fig. 3 The top panels are SCUBA maps at wavelengths 450 μm (*left*) and 850 μm (*right*). The middle panels are PACS 70 μm (*left*) and 160 μm (*right*), and the bottom panels are SPIRE 250 μm (*left*) and 350 μm (*right*). For comparison, all maps are overlaid with contours of CO(1–0) integrated intensity from the IRAM Plateau de Bure interferometer (Casoli et al. 1999). The contour levels are 1.0, 2.5, 4.0, 5.5, 7.0 and 8.5 Jy $\mathrm{km\ s^{-1}}$.

most of the dust and molecular gas emissions come from the central region of Arp 299.

We fit the SED for each source as well for the Arp 299 system to derive the physical parameters (i.e. temperature and mass) of the dust. The resolutions of SCUBA 450 and 850 μm are $7.5'' \times 7.5''$ and $14.5'' \times 14.5''$, respectively. The PACS resolutions for 70 and 160 μm are $5.76'' \times 5.46''$ and $10.65'' \times 12.13''$, respectively. The SPIRE resolutions for 250, 350 and 500 μm are $18'' \times 17''$, $25'' \times 23''$ and $37'' \times 34''$, respectively. From Figure 3, we can see that in the SPIRE 250 μm data (the left panel at the bottom) the overlap region between source A and source B + C was not resolved well. Furthermore, the SPIRE 350 μm data and 500 μm data have even lower resolution, and it is hard to distinguish between IC 694 and NGC 3690 on these maps. Thus we only use the SCUBA 450, 850 μm data and the PACS 70, 160 μm data to fit the SED function for IC 694 and NGC 3690. Figure 3 also shows that source B has a region that is overlapped with source C and cannot be resolved very well, so we fit the region of source B+C.

Finally, we use a circle with a diameter of $44''$, which is bigger than the resolution of all the observed data sets, to calculate the flux of Arp 299. From the maps

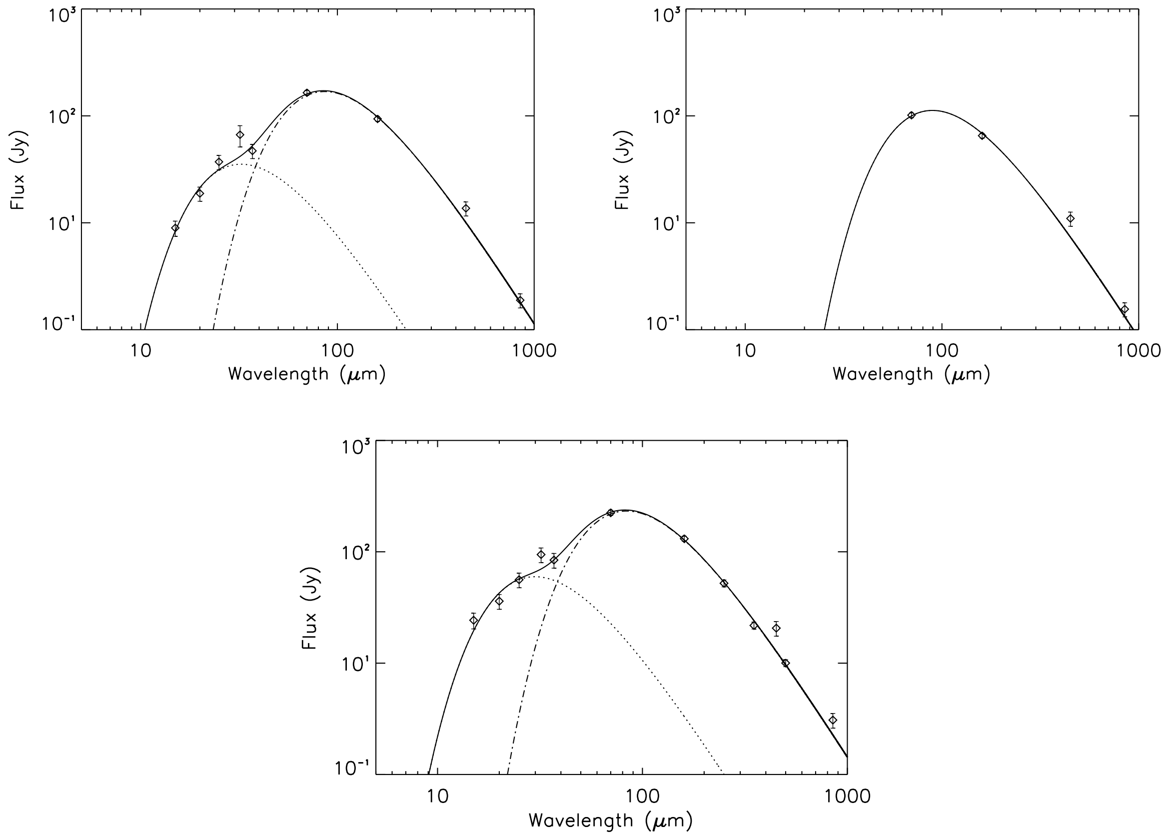

Fig. 4 *Upper-left panel*: the SED fitting result of source A. *Upper-right panel*: the SED fitting result of source B + C. *Bottom panel*: the SED fitting result of Arp 299. The dotted lines represent the warm component, the dot-dashed lines represent the cold component and the solid lines are the best SED fitting results.

in Figure 3, we can see that most of the dust emissions originate in this circle. The aperture correction factors for SCUBA 450 μm and SCUBA 850 μm are both 0.94 at diameter $44''$ (Dempsey et al. 2013). The aperture correction factors are 0.87 and 0.82 for PACS 70 μm and PCAS 160 μm (Balog et al. 2014), and 1.26, 1.31 and 1.80 for SPIRE 250 μm, SPIRE 350 μm and SPIRE 500 μm at diameter $44''$, respectively. When calculating the flux of source A and source B + C, we used circles with diameter $22''$.

The aperture correction factors are both 0.75 for SCUBA 450 μm and SCUBA 850 μm at diameter $22''$ (Dempsey et al. 2013). The aperture correction factors are 0.79 and 0.65 for PACS 70 μm and PCAS 160 μm (Balog et al. 2014), respectively. The measured fluxes of individual regions are presented in Table 1. Zhu et al. (2003, 2007) have pointed out that the CO(3–2) line has significant contamination on the SCUBA $850\,\mu$m continuum fluxes. Such contamination can be estimated using the formula: $S_{\rm CO} = 0.53 \times I_{\rm CO}\ {\rm mJy\ beam^{-1}\ (K\ km\ s^{-1})^{-1}}$. This yields an average $25\% - 30\%$ flux correction for the Arp 299 system. Thus we apply 75% of the SCUBA $850\,\mu$m fluxes and use the corrected fluxes for the SED fitting.

Meanwhile, we also use the mid-infrared data of 15, 20, 25, 32 and 37 μm (Charmandaris et al. 2002, table 1) to model the warm dust. The fluxes at 15, 20, 25, 32 and 37 μm for source A are 1.86, 5, 12.40, 27.0 ± 8.0 and 17.0 Jy, respectively, with 20% errors except for the 32 μm data. Note that mid-infrared data were not available for NGC 3690. The fluxes at 15, 20, 25, 32 and 37 μm for Arp 299 are 7.037, 11.90, 21.50, 43.00 and 36.96 Jy, respectively, with 20% errors. Assuming a Gaussian beam pattern for these mid-infrared data (Latvakoski et al. 1999), we can then ignore their aperture corrections. The mid-infrared fluxes mostly come from the warm and hot dust, which is usually distributed in the nuclear region of the galaxy. As shown in Section 3.2, we found that most of the warm dust component is located in the central $8''$ region of

Table 1 Fluxes, Dust Masses and Temperatures of Galaxies

Position	S_{70} (Jy)	S_{160} (Jy)	S_{250} (Jy)	S_{350} (Jy)	S_{450} (Jy)	S_{500} (Jy)	S_{850} (Jy)	$T_{\rm warm}$ (K)	$T_{\rm cold}$ (K)	$M_{\rm warm}$ ($10^4\,M_\odot$)	$M_{\rm cold}$ ($10^7\,M_\odot$)
A	90.22	42.57			3.27		0.31	89 ± 6	34 ± 1	6.0 ± 3.0	6.5 ± 0.8
B + C	47.35	26.27			2.44		0.24		33 ± 1		4.5 ± 0.6
Arp 299	136.20	66.59	19.49	6.09	5.66	2.16	0.60	97 ± 7	35 ± 1	8.1 ± 4.0	8.5 ± 0.6

IC 694. Thus here we assume most of the mid-infrared fluxes are distributed inside the circles used for the SED fitting. The fitted SED function is

$$S_\upsilon = \frac{M_{\rm warm}B(\upsilon, T_{\rm warm})k_\upsilon + M_{\rm cold}B(\upsilon, T_{\rm cold})k_\upsilon}{D^2}, \quad (1)$$

where S_υ is the flux at frequency υ, M is the dust mass, $D = 46\,{\rm Mpc}$ is the distance, k_υ is the absorption cross section per unit dust mass from Draine (2003) with $R_v = 3.1$. $B(\upsilon, T_{\rm warm})$ and $B(\upsilon, T_{\rm cold})$ are the related Plank functions

$$B(\upsilon, T) = \frac{2h\upsilon^3}{c^2}\frac{1}{\exp(h\upsilon/kT) - 1}. \quad (2)$$

Figure 4 presents the SED fitting results of source A (upper-left panel), source B + C (upper-right panel) and Arp 299 (bottom panel). For source A, the dust emissions have two components, a warm dust component with temperature 89 ± 6 K and mass $(6.0 \pm 3.0) \times 10^4\,M_\odot$, and a cold dust component with temperature 34 ± 1 K and mass $(6.5 \pm 0.8) \times 10^7\,M_\odot$. Because fewer data are available for source B + C, we fit the SED with a one-component model, which has a temperature 33 ± 1 K and dust mass $(4.5 \pm 0.6) \times 10^7\,M_\odot$. For Arp 299, a two-component model, consisting of a warm dust component with temperature 97 ± 7 K and dust mass $(8.1 \pm 4.0) \times 10^4\,M_\odot$, and a cold dust component with temperature 35 $\pm$ 1 K and mass $(8.5 \pm 0.6) \times 10^7\,M_\odot$, provides a good fit. The results are listed in Table 1.

Rosenberg et al. (2014) used a dust model with three-components to fit the SED of Arp 299, and they gave a temperature 29.1 ± 3.5 K and mass $1.1 \times 10^8\,M_\odot$ for the cool component. For the warm component and hot component, they showed the temperatures are 60.6 ± 4.9 K and 239.4 ± 22.7 K, and masses are $2.9 \times 10^6\,M_\odot$ and 141 $M_\odot$, respectively. Their hot dust component has very low mass and contributes very little to the mass budget of the whole system. Our results are consistent with their model with similar masses and temperatures for the cool components. Our results demonstrate that the majority of the dust mass comes from the cold dust component, but warm dust is necessary to explain the strong far-infrared (FIR) and submillimeter emission from this infrared luminous starbursting system.

3.2 The Warm Dust Component

In this section, we use the Herschel PACS 70 μm data to trace the distribution of the warm dust component on Arp 299. We further use the S_{70}/S_{450} ratio to identify the dust temperature of the warm dust component. The Herschel data have been convolved to $7.5''$ using the convolution kernels and programs described in Aniano et al. (2011) in order to match the resolution of the SCUBA 450 μm map. These are the highest resolution FIR and submillimeter data available for this system.

Figure 5 shows the contours of the S_{70}/S_{450} ratio overlaid on the S_{70}/S_{450} ratio map (upper-left panel), near-IR image at the K band (upper-right panel; Hibbard & Yun 1999) and PACS image at 70 μm (bottom panel). Higher S_{70}/S_{450} ratios indicate higher dust temperatures. The NIR K band image clearly shows the location of the two nuclei IC 694 and NGC 3690. We can see that most of the warm dust emissions comes from the central region of IC 694 with a radius $\sim\ 4''$, barely resolved at SCUBA 450 μm. Warm dust also exists in the galaxy NGC 3690, and the dust temperature on the southern disks appears to be slightly higher than that on the northern disks. However, the S/Ns of SCUBA 450 μm data are relatively low in these regions, thus we should be cautious when interpreting these data.

The PACS 70 μm (Fig. 5 bottom panel) map has a resolution of $5.8''$ and it clearly shows that most of the warm/hot dust is very centrally distributed around the nucleus of IC 694. This region also hosts the strongest CO(1–0) peak as shown in Figure 3. The strong mid-IR and FIR emissions indicate intense starburst activity at the nucleus. The physical conditions of molecular gas in this region are crucial in understanding the star formation and AGN activities of this merging system.

3.3 Physical Conditions of the Molecular Gas

As already shown in Figures 1 and 2, we have observed six points at CO(4–3) and 13 points at the CO(3–2) transition. We use the conversion factor $S = 15.625/\eta_{\rm a}T_{\rm a}^*\,{\rm Jy\,K^{-1}}$ to convert the flux unit from ${\rm K\,km\,s^{-1}}$ to ${\rm Jy\,km\,s^{-1}}$. The conversion factors are 25.2 and 50.4 for CO(3–2)and CO(4–3) with the $\eta_{\rm a}$ equal to

Table 2 Comparison of the Observed Fluxes of Source A

Source A	P5	P1	P6	P10
CO(3–2) Flux ($\mathrm{K\,km\,s^{-1}}$)	36.30	26.26	53.47	48.92
PACS 70 μm (Jy)	63.48	44.43	78.10	48.60
CO(3–2)/Pacs70	0.57	0.59	0.68	1.01

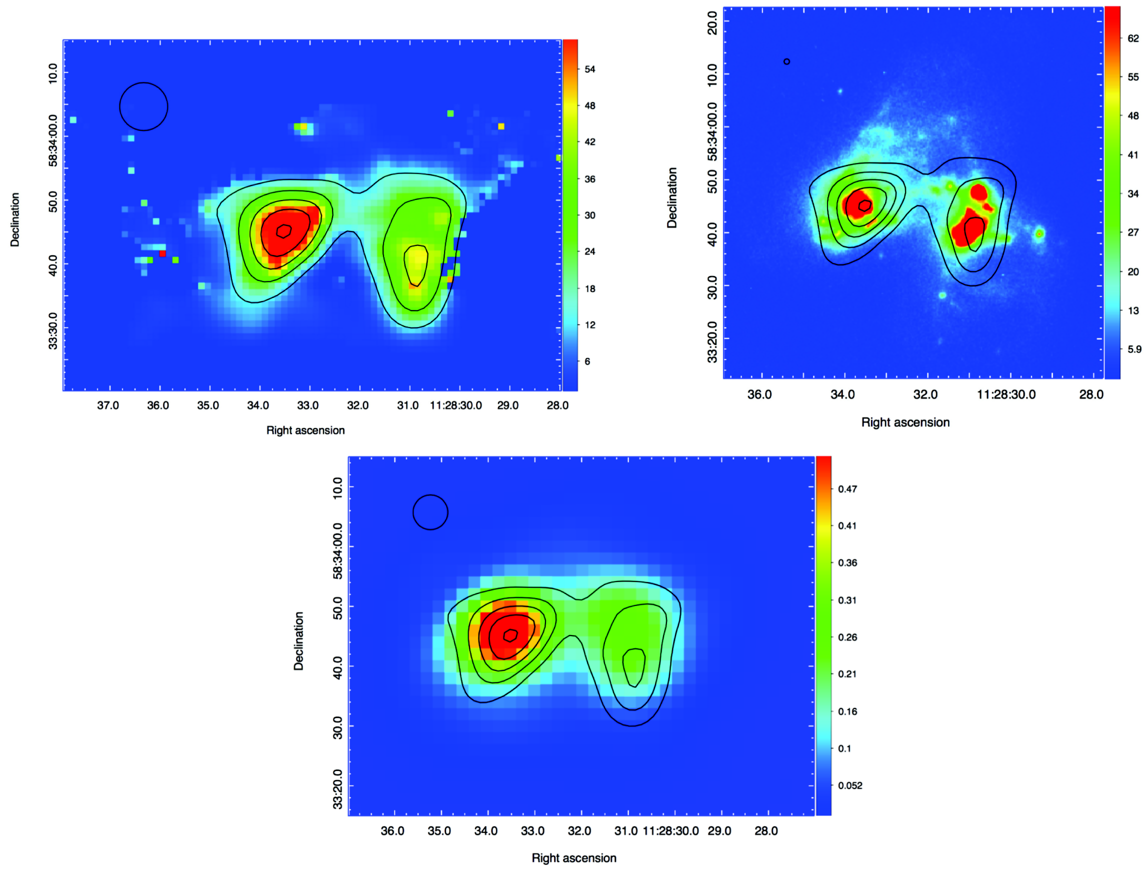

Fig. 5 The maps of S_{70}/S_{450}, K band map and PACS 70 μm map with contours of S_{70}/S_{450}. The contours are 13, 26, 40, 53 and 67. Upper-left panel is the color representation of S_{70}/S_{450} with beam resolution of 7.5″. Upper-right panel is the K band map (Hibbard & Yun 1999, observed with the University of Hawaii 88 inch telescope) with beam resolution of 1″. Bottom panel is the PACS 70 μm map and its beam resolution is 5.8″.

0.62 and 0.31 for the JCMT CO(3–2) and CO(4–3) receivers, respectively. The pointing centers of the CO(3–2) observations are offset from the centers of sources A, B and C, hence we estimate the CO(3–2) fluxes of these sources by assuming that the CO(3–2) fluxes have a constant ratio with respect to the PACS 70 μm fluxes at each source. When calculating the ratio, we smoothed the resolution of the PACS 70 μm map to match the resolution of the CO(3–2) map. The detailed values are shown in Tables 2 and 3.

Table 2 shows that source A has almost constant ratios except for the point P10, which may be caused by pointing errors. We adopt a ratio of $0.63{\pm}0.08$ using the mean value of points P5 and P6 (which are close to the center of source A), and then estimate the CO(3–2) flux of source A as 1233 $\mathrm{Jy\,km\,s^{-1}}$ within the CO(3–2) beam (14″).

Table 3 shows that for sources B and C, the flux ratios are roughly constant at about $1.07{\pm}0.04$ (mean value of points P3, P4, P8 and P9) and 0.97 ± 0.19 (mean value of points P12 and P13), respectively. Thus the CO(3–2) fluxes of sources B and C are estimated as 833 $\mathrm{Jy\,km\,s^{-1}}$ and 627 $\mathrm{Jy\,km\,s^{-1}}$ within a diameter of 14″, respectively. The results are listed in Table 4.

Sliwa et al. (2012) applied the radiative transfer code RADEX (van der Tak et al. 2007) to estimate the physical properties in the system using the CO(3–2), CO(2–1) and CO(1–0) transitions. They found that IC 694 and

Table 3 Comparison of the Observed Fluxes of Sources B and C

Source B/C	P2	P3	P4	P7	P8	P9	P11	P12	P13
CO(3–2) Flux (K km s^{-1})	24.71	16.41	17.5	44.35	29.83	32.27	25.33	21.14	28.27
PACS 70 μm (Jy)	15.13	11.06	11.23	29.40	21.27	24.28	14.33	15.85	21.85
CO(3–2)/Pacs70	0.89	1.00	1.12	0.95	1.08	1.07	0.94	1.10	0.84

Table 4 Center Fluxes for Galaxies in Arp 299

Position	RA	Dec	CO(4–3) Flux (Jy km s^{-1})	CO(3–2) Flux (Jy km s^{-1})
A	$11^{\rm h}28^{\rm m}33.6^{\rm s}$	$58°33'47''$	2200 ± 220	1233 ± 180
B	$11^{\rm h}28^{\rm m}31^{\rm s}$	$58°33'41''$		833 ± 107
C	$11^{\rm h}28^{\rm m}31^{\rm s}$	$58°33'50''$		627 ± 139

Table 5 Observed Fluxes and Flux Ratios of Arp 299

Position	RA	Dec	CO(11–10) Flux (Jy km s^{-1})	CO(13–12) Flux (Jy km s^{-1})	$I_{\rm CO(11-10)}/I_{\rm CO(3-2)}$	$I_{\rm CO(13-12)}/I_{\rm CO(4-3)}$
A	$11^{\rm h}28^{\rm m}33^{\rm s}.7$	$58°33'46''$	1418 ± 60	1126 ± 60	0.14 ± 0.04	0.06 ± 0.01
B	$11^{\rm h}28^{\rm m}31^{\rm s}$	$58°33'41''$	479 ± 40	405 ± 38	0.07 ± 0.02	
C	$11^{\rm h}28^{\rm m}31.1^{\rm s}$	$58°33'48.2''$	488 ± 40	256 ± 40	0.10 ± 0.03	

NGC 3690 consist of two gas components with a wide range of physical parameters, from a warm moderately dense gas with kinetic temperature $T_{\rm kin} > 30\,{\rm K}$ and hydrogen density $n({\rm H_2}) \sim 0.3 - 3 \times 10^3\,{\rm cm^{-3}}$ to a cold dense gas with $T_{\rm kin} \sim 10 - 30\,{\rm K}$ and $n({\rm H_2}) > 3 \times 10^3\,{\rm cm^{-3}}$ (Sliwa et al. 2012). Based on the CO(3–2)/(1–0) and CO(4–3)/(1–0) ratios, Papadopoulos et al. (2012) estimate the range of $T_{\rm kin} = 30 - 40\,{\rm K}$ and $n({\rm H_2}) = 10^3 - 10^4\,{\rm cm^{-3}}$ using a one-phase large-velocity-gradient (LVG) model, and their best estimate is $T_{\rm kin} = 30\,{\rm K}$ and $n({\rm H_2}) = 10^4\,{\rm cm^{-3}}$. A moderately warm and dense gas is necessary to fit the CO(4–3) data. While the lowest J CO transitions can be fitted with a gas component with relatively low density and temperature, the high-J CO transitions can only be fitted with a gas density and a temperature range from medium to high (Rosenberg et al. 2014). Using the CO transition data from $J = 1$ to $J = 14$, Rosenberg et al. (2014) provided three photon-dominated region (PDR) models, in which the density of PDR I is in the range $10^{2.5} - 10^{5.5}\,{\rm cm^{-3}}$, that of PDR II is in the range $10^3 - 10^6\,{\rm cm^{-3}}$ and that of PDR III is in the range $10^5 - 10^6\,{\rm cm^{-3}}$. They showed that the only way to reproduce the flux of the high-J CO lines is with a PDR model with a density $10^6\,{\rm cm^{-3}}$ and a radiation field ${\rm G_0} = 10^6$, and the dust needs to be heated to a high temperature of $239.4 \pm 22.7\,{\rm K}$ as well (Rosenberg et al. 2014). Mashian et al. (2015) used a two component LVG model to fit the IC 694 galaxy with the CO transition data from $J = 1$ to $J = 20$, and they found that the two components have the same kinetic temperature of 200 K but different ${\rm H_2}$ number densities of $10^{3.4}$ and $10^{5.8}\,{\rm cm^{-3}}$ respectively.

Previous CO studies have indicated that there are at least two gas components in Arp 299, with different gas temperature and density ranges. Our own SED fitting of the dust emission also suggests at least two dust components as shown in Sections 3.1 and 3.2. The S_{70}/S_{450} ratio map shows that the majority of the hot dust is from the central region of IC 694 with a diameter $\sim 8''$. With our high resolution CO(4–3) and CO(3–2) data from JCMT, combined with the Herschel data at high-J CO transitions, we can have a better estimate of the physical parameters for the hot component of molecular gas traced by CO.

We assume that most of the high-J CO emissions are confined to a region similar to that of the hot dust, e.g. within the central $8''$ in diameter, which can be treated as point sources with respect to the beam sizes of SPIRE/FTS and PACS. The resolution of the SPIRE/FTS CO(11–10) data is similar to that of the JCMT CO(3–2) line, while the resolution of the SPIRE/FTS CO(13–12) is similar to that of JCMT CO(4–3). Then the flux ratios of CO(11–10) to CO(3–2), and CO(13–12) to CO(4–3) can be calculated directly without beam convolution. The resolution of the Herschel PACS CO(14–13) data is also similar to that of the JCMT CO(4–3) line, and thus we can derive the $I_{\rm CO(14-13)}/I_{\rm CO(4-3)}$ line ratio as 0.07 $\pm$ 0.02 for source A, using the flux value of 1824 $\pm$ 273 $\rm Jy\,km\,s^{-1}$ for CO(14–13) (Mashian et al. 2015). However, it is likely that the CO(4–3) and CO(3–2) fluxes have contributions from both the cold and hot components, thus we need to correct for contamination of the cold component in the CO(4–3) and (3–2) emissions when using them to constrain the parameters for the hot components. We assume the cold gas component has a gas temperature similar to that of the dust temperature, e.g. about 30 K. Then we can use the LVG solution of Papadopoulos et al. (2012) to estimate the parameters of the cold component as $T = 30\,{\rm K}$ and density $n = 10^4\,{\rm cm^{-3}}$. Using the RADEX code, we then estimate that about $15\% - 25\%$ of the CO(4–3) and $35\% - 45\%$ of the CO(3–2) flux comes from the cold component. After removing the contribution from the cold component, the flux ratio of $I_{\rm CO(11-10)}/I_{\rm CO(3-2)}$ should be corrected as 0.14 $\pm$ 0.04, the ratio of $I_{\rm CO(13-12)}/I_{\rm CO(4-3)}$ should be 0.06 $\pm$ 0.01 and the flux ratio of $I_{\rm CO(14-13)}/I_{\rm CO(4-3)}$ should be 0.08 $\pm$ 0.02. These values are listed in Table 5, and we will use them to estimate the physical parameters for the hot component.

Our data are fitted with a 3D-grid RADEX model with a line width of $150\,{\rm km\,s^{-1}}$, kinetic temperature $T_{\rm kin}$ range from 0 to 400 K, number density $n({\rm H_2})$ range from 10^2 to $10^7\,{\rm cm^{-3}}$ and column density N(CO) range from 10^{16} to $10^{20}\,{\rm cm^{-2}}$. The results show that the flux ratio is not sensitive to the column density N(CO). The fitting contours of $I_{\rm CO(11-10)}/I_{\rm CO(3-2)}$ (upper-left panel), $I_{\rm CO(13-12)}/I_{\rm CO(4-3)}$ (upper-right panel) and $I_{\rm CO(14-13)}/I_{\rm CO(4-3)}$ (bottom panel) with column density $2 \times 10^{17}\,{\rm cm^{-2}}$ are shown in Figure 6. Then the best fitting result is $n({\rm H_2}) = 10^{4.7} - 10^{5.5}\,{\rm cm^{-3}}$ and $T_{\rm kin} = 110 - 150\,{\rm K}$ according to the contours shown in Figure 6. Based on the RADEX RADEX_COLUMN program and the best fitting number density and kinetic temperature, the best fitting column density of molecular CO is in the range 2.0×10^{17} to $4.0 \times 10^{17}\,{\rm cm^{-2}}$.

The $\rm H_2$ column density is $N_{\rm H_2} = 6.7 \times 10^{20} - 1.33 \times 10^{21}\,{\rm cm^{-2}}$ according to equation $N_{\rm H_2} = N_{\rm CO}/x_{\rm CO}$, where $x_{\rm CO} = 3 \times 10^{-4}$ is the abundance factor (Ward et al. 2003). In combination with the radius of the warm/hot center region, we can conclude that the center warm/hot $\rm H_2$ mass is in the range 3.8×10^7 to $7.7 \times 10^7\,M_\odot$. Compared to the total $\rm H_2$ mass of $M_{\rm H_2} = 7 \pm 1 \times 10^8\,M_\odot$ for IC 694 (Sliwa et al. 2012), the warm/hot region contains 5.0%–15.0% of the total $\rm H_2$ mass for the region, indicating that most of the gas is cold and diffuse. Rigopoulou et al. (2002) found that the fraction of warm gas mass accounts for as much as 10% of the total galactic mass in starbursts and $2\% - 35\%$ in Seyferts, which is consistent with our result.

3.4 Kinematic Analysis

The gas in the central region of IC 694 has both a high temperature $T_{\rm kin}$ (range 110–150 K) and high density $n({\rm H_2})$ (range $10^{4.7} - 10^{5.5}\,{\rm cm^{-3}}$). Such conditions imply a high gas pressure. The outer region has a relatively low density $n({\rm H_2}) = 10^4\,{\rm cm^{-3}}$ and kinetic temperature $T_{\rm kin} = 30\,{\rm K}$ (Papadopoulos et al. 2012). To maintain hydrostatic equilibrium, we have

$$\frac{dp}{dr} = -\frac{G\rho(r)M_{\rm enc}(r)}{r^2}, \tag{3}$$

where $M_{\rm enc}(r)$ represents the enclosed mass at radius r, p is the pressure, dr is the thickness of the transition layer, G is the gravitational constant and $\rho(r)$ is the density of the gas at radius r. We can deduce that

$$\begin{aligned} dp &= nkT_{\rm cold} - nkT_{\rm warm/hot} \\ &= -nkT_{\rm warm/hot}, \end{aligned} \tag{4}$$

where n is the number density, k is the Boltzmann constant, $T_{\rm warm/hot}$ is the temperature of the warm/hot gas and $T_{\rm cold}$ is the temperature of the cold gas. The warm/hot temperature is 110 K, the density n is $10^{5.5}\,{\rm cm^{-3}}$ and the number density is $10^4\,{\rm cm^{-3}}$ for $\rho(r)$. Assuming the thickness of the transition layer dr is about $1/10r$, then the mass that is required to maintain hydrostatic equilibrium is $\sim 5.5 \times 10^7\,M_\odot$ at the $4''$ radius of the warm/hot gas region (assuming a distance of 46 Mpc). If the thickness is smaller, then the required mass of the warm/hot gas will be larger. This value is similar to the total mass of the warm/hot gas component we estimated with the RADEX model ($3.8 \times 10^7 - 7.7 \times 10^7\,M_\odot$). Considering other mass components such as stellar mass, there appears to be enough mass to provide the gravity necessary to confine the central hot and dense gas against thermal pressure to maintain hydrostatic equilibrium. Thus the hot gas component could be stable and could last for a long time at the nucleus of IC 694.

3.5 Infrared Luminosity and Star Formation Rate

The infrared luminosities $L_{\rm IR}(8 - 1000\,\mu{\rm m})$ are derived from the SED fitting results, and are shown in Table 6. The star formation rates (SFRs) can be deduced

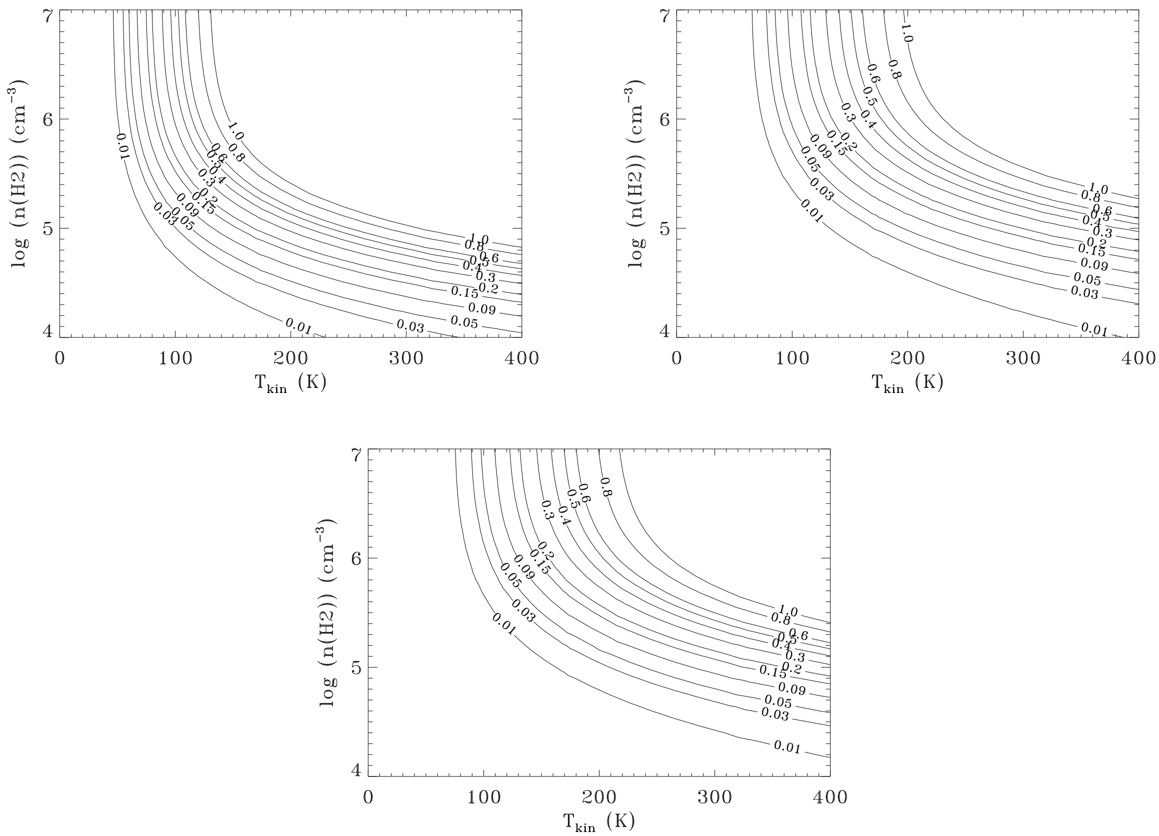

Fig. 6 Contours calculated with the RADEX model with column density $2 \times 10^{17}\,\mathrm{cm}^{-2}$. Upper-left panel displays contours of $I_{\mathrm{CO(11-10)}}/I_{\mathrm{CO(3-2)}}$ with kinetic temperature T_{kin} and hydrogen density $n(\mathrm{H}_2)$. Upper-right panel shows contours of $I_{\mathrm{CO(13-12)}}/I_{\mathrm{CO(4-3)}}$ and bottom panel features contours of $I_{\mathrm{CO(14-13)}}/I_{\mathrm{CO(4-3)}}$.

from infrared luminosities by using the equation below (Kennicutt 1998)

$$\begin{aligned}\mathrm{SFR}(M_\odot\,\mathrm{yr}^{-1}) &= 4.5 \times 10^{-44} L_{\mathrm{IR}}(\mathrm{erg\,s}^{-1}) \\ &= 1.7307 \times 10^{-10} L_{\mathrm{IR}}\,(L_\odot), \quad (5)\end{aligned}$$

with $L_\odot = 3.846 \times 10^{33}\,\mathrm{erg\,s}^{-1}$. The resulting SFR is $86.5\,M_\odot\,\mathrm{yr}^{-1}$ for source A and $36.3\,M_\odot\,\mathrm{yr}^{-1}$ for source B + C based on Equation (5). The SFR of Arp 299 is $150.5\,M_\odot\,\mathrm{yr}^{-1}$, much higher than the result of Sliwa ($70\,M_\odot\,\mathrm{yr}^{-1}$), which may be associated with the different methods of calculating infrared luminosities. In previous studies, L_{IR} was calculated by using IRAS S_{60} μm and S_{100} μm data due to the lack of submillimeter data. Thanks to the Herschel and SCUBA data, we can model the SED more accurately now, which leads to more accurate integrated infrared luminosities and SFRs. For source B + C, the one component model may underestimate the infrared luminosity and the SFR. For comparison, the SFR is $5\,M_\odot\,\mathrm{yr}^{-1}$ in the Milky Way (Smith et al. 1978), so the SFR in Arp 299 is significantly higher than that in normal galaxies.

Table 6 Luminosity and SFR for Each Galaxy

Position	L_{IR} ($10^{11}\,L_\odot$)	SFR ($M_\odot\,\mathrm{yr}^{-1}$)
A	5.0 ± 3.2	86.5 ± 55.3
B + C	2.1 ± 1.6	36.3 ± 27.7
Arp 299	8.7 ± 5.7	150.5 ± 98.6

4 SUMMARY AND CONCLUSIONS

We present the observed JCMT CO(3–2) and CO(4–3), and SCUBA 850 and 450 μm data, as well as the fully-sampled Herschel 500, 350, 250, 160 and 70 μm continuum maps of Arp 299. Combined with the mid-infrared data at 5, 20, 25, 32 and 37 μm (Charmandaris et al. 2002), we fit the SED of the dust emission and find that there are at least two dust components (a cold component and a warm component) in source A and Arp 299. We find that most of the dust is cold, and warm dust accounts for a small amount of the total dust mass. The high resolution S_{70}/S_{450} ratio map shows that the warm/hot dust is mostly distributed in the central region of source A with radius $\sim 4''$.

By combining the Herschel CO(11–10), CO(13–12) and CO(14–13) data with the JCMT CO(3–2) and CO(4–3) data, which have similar spatial resolution and beam size, we have used a RADEX model to calculate the parameters for the warm/hot molecular gas component in the center of IC 694. We estimate that $T_{\rm kin}$ is in the range of 110 to 150 K and $n(\rm H_2) = 10^{4.7} - 10^{5.5}\,cm^{-3}$. The mass of the warm/hot gas $M(\rm H_2)$ is $3.8 \times 10^7 - 7.7 \times 10^7\,M_\odot$, which accounts for 5.0%$-$15.0% of the total H_2 mass of IC 694. The star formation rate is 86.5 $M_\odot\,\rm yr^{-1}$ for source A, 36.3 $M_\odot\,\rm yr^{-1}$ for source B + C, and 150.5 $M_\odot\,\rm yr^{-1}$ for Arp 299.

Acknowledgements The authors wish to thank the JCMT staff for their generous assistance during the observations. We thank Dr. Padelis P. Papadopoulos for valuable suggestions and also for sharing his JCMT data. We also thank Dr. Christina Strom and Dr. Yinghe Zhao for their suggestions and comments. This work is partly supported by the China Ministry of Science and Technology under the State Key Development Program for Basic Research (2012CB821800). This work is supported by the Joint Research Fund in Astronomy (U1531246) under cooperative agreement between the National Natural Science Foundation of China (NSFC) and the Chinese Academy of Sciences (CAS) and also supported by the Strategic Priority Research Program "The Emergence of Cosmological Structures" of the Chinese Academy of Sciences (Grant No. XDB09000000).

References

Aalto, S., Johansson, L. E. B., Booth, R. S., & Black, J. H. 1991, A&A, 249, 323

Alonso-Herrero, A., Rieke, G. H., Rieke, M. J., & Scoville, N. Z. 2000, ApJ, 532, 845

Aniano, G., Draine, B. T., Gordon, K. D., & Sandstrom, K. 2011, PASP, 123, 1218

Balog, Z., Müller, T., Nielbock, M., et al. 2014, Experimental Astronomy, 37, 129

Bertincourt, B., Lagache, G., Martin, P. G., et al. 2016, A&A, 588, A107

Carolan, P. B., Khanzadyan, T., Redman, M. P., et al. 2009, MNRAS, 400, 78

Casoli, F., Dupraz, C., & Combes, F. 1992, A&A, 264, 55

Casoli, F., Willaime, M.-C., Viallefond, F., & Gerin, M. 1999, A&A, 346, 663

Charmandaris, V., Stacey, G. J., & Gull, G. 2002, ApJ, 571, 282

Dempsey, J. T., Friberg, P., Jenness, T., et al. 2013, MNRAS, 430, 2534

Draine, B. T. 2003, ARA&A, 41, 241

Gallais, P., Laurent, O., Charmandaris, V., et al. 1999, in ESA Special Publication, 427, The Universe as Seen by ISO, eds. P. Cox & M. Kessler, 881

García-Marín, M., Colina, L., Arribas, S., Alonso-Herrero, A., & Mediavilla, E. 2006, ApJ, 650, 850

Gehrz, R. D., Sramek, R. A., & Weedman, D. W. 1983, ApJ, 267, 551

Griffin, M. J., Abergel, A., Abreu, A., et al. 2010, A&A, 518, L3

Hibbard, J. E., & Yun, M. S. 1999, AJ, 118, 162

Jenness, T., & Lightfoot, J. F. 1998, in Astronomical Society of the Pacific Conference Series, 145, Astronomical Data Analysis Software and Systems VII, eds. R. Albrecht, R. N. Hook, & H. A. Bushouse, 216

Kennicutt, Jr., R. C. 1998, ARA&A, 36, 189

Latvakoski, H. M., Stacey, G. J., Gull, G. E., & Hayward, T. L. 1999, ApJ, 511, 761

Mashian, N., Sturm, E., Sternberg, A., et al. 2015, ApJ, 802, 81

Nielbock, M., Müller, T., Klaas, U., et al. 2013, Experimental Astronomy, 36, 631

Papadopoulos, P. P., van der Werf, P. P., Xilouris, E. M., et al. 2012, MNRAS, 426, 2601

Pilbratt, G. L., Riedinger, J. R., Passvogel, T., et al. 2010, A&A, 518, L1

Poglitsch, A., Waelkens, C., Geis, N., et al. 2010, A&A, 518, L2

Rigopoulou, D., Kunze, D., Lutz, D., Genzel, R., & Moorwood, A. F. M. 2002, A&A, 389, 374

Rosenberg, M. J. F., Meijerink, R., Israel, F. P., et al. 2014, A&A, 568, A90

Sanders, D. B., Mazzarella, J. M., Kim, D.-C., Surace, J. A., & Soifer, B. T. 2003, AJ, 126, 1607

Sliwa, K., Wilson, C. D., Petitpas, G. R., et al. 2012, ApJ, 753, 46

Smith, L. F., Biermann, P., & Mezger, P. G. 1978, A&A, 66, 65

Soifer, B. T., Sanders, D. B., Madore, B. F., et al. 1987, ApJ, 320, 238

van der Tak, F. F. S., Black, J. H., Schöier, F. L., Jansen, D. J., & van Dishoeck, E. F. 2007, A&A, 468, 627

Ward, J. S., Zmuidzinas, J., Harris, A. I., & Isaak, K. G. 2003, ApJ, 587, 171

Wynn-Williams, C. G., Hodapp, K.-W., Joseph, R. D., et al. 1991, ApJ, 377, 426

Zhu, M., Gao, Y., Seaquist, E. R., & Dunne, L. 2007, AJ, 134, 118

Zhu, M., Seaquist, E. R., & Kuno, N. 2003, ApJ, 588, 243